

SIRe-IR: Inverse Rendering for BRDF Reconstruction with Shadow and Illumination Removal in High-Illuminance Scenes

Ziyi Yang¹ Yanzhen Chen¹ Xinyu Gao¹ Yazhen Yuan² Yu Wu²
 Xiaowei Zhou¹ Xiaogang Jin^{1†}

¹State Key Laboratory of CAD&CG, Zhejiang University ²Tencent

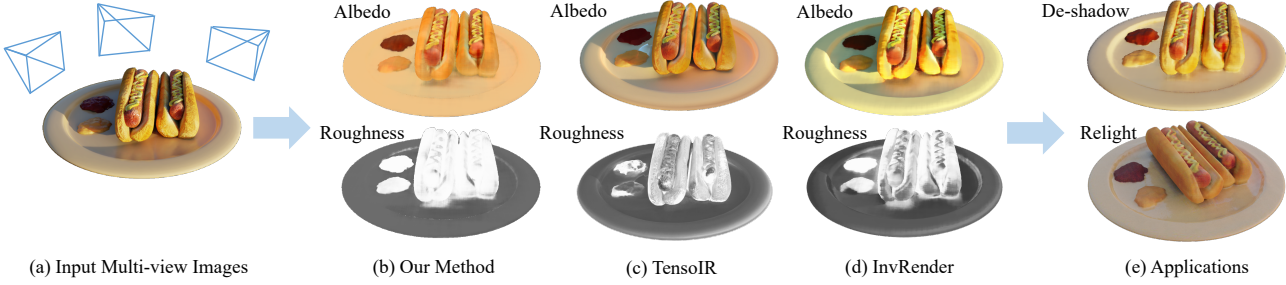


Figure 1. Given a set of multi-view images and corresponding camera poses (a), our proposed method, *SIRe-IR*, can reconstruct accurate scene geometry and decompose high-quality light **without baking shadow and indirect illumination** into the albedo and roughness (b). In most scenes with intense illumination and shadows, we show that *SIRe-IR* outperforms TensoIR [17] (c) and *Invrender* [57] (d). As a result, our method is suitable for free-viewpoint relighting and shadow-free scene rendering (e).

Abstract

<https://github.com/ingra14m/SIRe-IR>.

Implicit neural representation has opened up new possibilities for inverse rendering. However, existing implicit neural inverse rendering methods struggle to handle strongly illuminated scenes with significant shadows and indirect illumination. The existence of shadows and reflections can lead to an inaccurate understanding of scene geometry, making precise factorization difficult. To this end, we present SIRe-IR, an implicit neural inverse rendering approach that uses non-linear mapping and regularized visibility estimation to decompose the scene into environment map, albedo, and roughness. By accurately modeling the indirect radiance field, normal, visibility, and direct light simultaneously, we are able to remove both shadows and indirect illumination in materials without imposing strict constraints on the scene. Even in the presence of intense illumination, our method recovers high-quality albedo and roughness with no shadow interference. SIRe-IR outperforms existing methods in both quantitative and qualitative evaluations. We will release our code at

1. Introduction

Inverse rendering, the task of extracting the geometry, materials, and lighting of a 3D scene from 2D images, is a longstanding challenge in computer graphics and computer vision. Previous methods, such as providing geometry for the entire scene [34, 46], modeling shape representation [14, 22, 33, 53] or pre-providing multiple known light information [12], have achieved plausible results using prior information. To achieve clear albedo and roughness decomposition, factors such as light obscuration, reflection, or refraction must be taken into account. Among these, hard and soft shadows are particularly challenging to eliminate, as they play a critical role not only in obtaining cleaner material but also in accurately modeling geometry and light sources. Some data-driven approaches [23, 39] have performed plausible shadow removal at the image level. However, these methods are not generally applicable for inverse rendering.

Since the advent of NeRF [31], implicit neural represen-

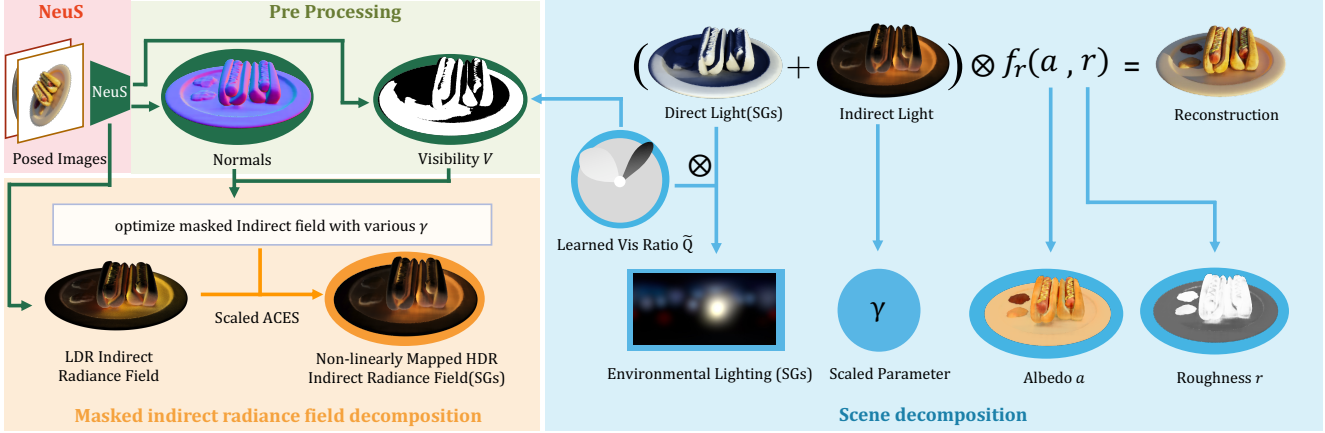


Figure 2. **The pipeline of our SIRE-IR.** During the NeuS stage, we reconstruct the scene as an implicit representation by NeuS [47]. From the implicit representation, we extract normal (MLPs), indirect radiance field (SGs), and visibility V (MLPs). Next, by taking ACES tone mapping into account, we train a masked non-linearly mapped indirect radiance field with visibility and randomly sampled γ values. During scene decomposition, we optimize learnable parameters, including environmental lighting, scaled parameter γ , albedo a , and roughness r , to minimize reconstruction loss under the constraint of the rendering equation. To reduce the stubborn visibility errors caused by reflection, we employ a learnable visibility ratio of direct SGs, \tilde{Q} , and perform regularized visibility estimation on V to obtain more accurate visibility, which is critical for eliminating shadows at the edges and boundaries.

tation has garnered significant interest in portraying scenes as neural radiance fields. Furthermore, the high-quality geometry and radiance fields modeled by NeRF are exceptionally useful for *inverse rendering*. By applying implicit neural representation to inverse rendering [4, 19, 55], plausible factorization can be achieved in simple scenes with weak light intensity. Thanks to NeRFactor [56] and its relevant work [10], which extend previous works by explicitly representing visibility, implicit inverse rendering can be improved with simple shadow removal and clear edge in albedo and roughness. Recently, InvRender [57] has taken the scene factorization problem to a new level by modeling indirect illumination, serving as the baseline in our experiment.

The current methods for implicit neural inverse rendering mentioned above have shown limitations when dealing with scenarios with intense illumination and strong shadow, which are common in real environments. To deal with such scenes, the following challenges arise in order to obtain clear PBR materials.

First, previous methods for inverse rendering have faced the challenge in separating complex light phenomena such as reflection and obscuration in low dynamic range (LDR) space. While these methods perform well for scenes with weak light intensity, they struggle to accurately decompose albedo and roughness in scenarios with intense lighting. As shown in Fig. 1, both shadow and indirect illumination remain in the albedo. According to the rendering equation, decreasing the intensity of direct and indirect illumination in the shadow area is required to remove shadows, while increasing the intensity of indirect illumination is necessary

to eliminate the remaining indirect light in the albedo. To address the aforementioned challenge, we propose a novel approach that explicitly applies a non-linear mapping function on the indirect radiance field to non-linearly and monotonically map the 0-1 value of indirect illumination intensity into a wider range and enhance the color contrast. Specifically, we propose a ACES tone mapping search algorithm that can automatically learn the appropriate mapping curve for a specific scene, eliminating the need for additional parameters such as camera exposure time.

Second, previous approaches have not adequately modeled decomposed components. For example, the discontinuous indirect radiance field has difficulty accurately converging based on smooth spherical Gaussians (SGs), particularly in scenes with intense directional lighting. Additionally, modeling discontinuous and high-frequency visibility requires a high-frequency function, which is difficult for multilayer perceptron (MLP) to accurately fit. Our approach accurately models the indirect radiance field and visibility simultaneously by introducing a novel masked indirect radiance field. This enables us to better remove indirect illumination without strong constraints on the scene.

Third, previous training strategies struggle with convergence stability due to the vast number of learning parameters. As a result, we incorporate a prior assumption that “the visibility ratio [57] of a specific point x from a given direct SG is smooth” and employ regularized visibility estimation to obtain more precise visibility. This aids in the decomposition of scenes into environment maps, albedo, and roughness with effective shadow removal.

In summary, the major contributions of our work are:

- A novel non-linearly mapped indirect radiance field for the inverse rendering task. It enables the production of clean albedo and roughness in scenes with intense lighting and strong shadows, allowing for the creation of high-quality visual content.
- A novel masked indirect light representation that uses smooth spherical Gaussians and a binary classification visibility network to effectively model high-frequency visibility and discontinuous indirect light.
- A novel regularized visibility estimation that uses an intermediate layer to optimize the visibility. It decreases shadow residue on edges and improves the convergence stability of the ill-posed inverse rendering task.

2. Related Work

2.1. Inverse Rendering

Inverse rendering is a process in computer graphics that aims to derive an understanding of the physical properties of a scene from a set of images. Because the problem is highly ill-posed, most previous works have incorporated priors such as illumination, shape, and shadow, as well as additional observations such as scanned geometry [21, 34, 38] and known light conditions [12], to ensure proper regularization during the optimization process of the rendering components. Simplified approaches, such as those assuming outdoor and natural light [40] or white light [29], aim to reduce the number of fitting parameters in an ill-posed problem. Recently, data-driven methods [2, 7, 24, 37, 39, 52] have focused on decomposing scene information from a single or two-shot image(s), heavily relying on geometric priors and training complexity. In contrast, our research focuses on a more general decomposition framework that reduces the model’s reliance on specialized equipment and scene complexity while also improving model generalization through more efficient use of geometric prior.

2.2. Implicit Neural Representation

Neural rendering has gained popularity due to its ability to produce photorealistic images. Recently, NeRF [31] enables photo-realistic novel view synthesis using MLPs. It can handle complex light scattering and reconstruct high-quality scenes for downstream tasks.

Subsequent work has enhanced NeRF’s efficiency in various ways, elevating it to new heights and enabling its use in other domains. Structure-based techniques [11, 13, 15, 36, 51] have explored ways to improve inference or training efficiency by caching or distilling implicit neural representation into the efficient data structure. Hybrid methods [9, 25, 27, 42, 43] aim to improve the efficiency by incorporating explicit voxel-based data structures. Among them, Instant-NGP [32] achieves minute training by additionally incorporating hash encoding.

In addition, some follow-up methods [35, 47, 50] are dedicated to recovering clear surfaces for scenes with complex solid objects by modeling a learnable SDF network, the value of which indicates the minimum distance between the input coordinate and surfaces in the scene. In our work, we show that the simple and continuously differentiable nature of SDF makes it suitable for learning geometry priors in inverse rendering. Furthermore, drawing inspiration from PlenOctree [51], we construct an octree tracer from the SDF to improve inference efficiency and accuracy compared to sphere tracing.

2.3. Implicit Neural Inverse Rendering

In recent years, there has been a surge of interest in implicit inverse rendering, building on the success of NeRF and its fully differentiable implicit neural representation. To model spatially-varying bidirectional reflectance distribution function (SVBRDF) under more casual capture conditions, many recent methods [4–6, 19, 49, 54] have relied on implicit representation. Other works [17, 26, 41, 48, 56] have focused on physical-based modeling for complex scenes via visibility prediction. L-Tracing [10] introduced a new algorithm for estimating visibility without training, while NeRFactor [56] proposed a canonical normal and BRDF smoothness to address NeRF’s poor geometric quality, which is critical to the decomposition stage.

Inverse Rendering with dynamic light [20] has also shown promise by exploiting illumination differences between input images and decomposing them into multiple low-rank principal components. In contrast, our work focuses on a more arbitrary but static light condition.

Our work builds on recent advancements in implicit volumetric representation to achieve greater inverse rendering capability than previous methods. In particular, we draw inspiration from PhySG [55], which improved the modeling of high-reflectivity materials by using SGs to represent environment illumination, and InvRender [57], which extends previous work by modeling indirect illumination.

2.4. Rendering Equation

The rendering equation proposed by [18] is a fundamental equation in computer graphics that describes the physical processes of light transport in a scene. It can be used to simulate complex lighting effects such as reflections, refractions, and global illumination:

$$L_o(\mathbf{x}, \omega_o) = L_e(\mathbf{x}, \omega_o) + \int_{\Omega} f_r(\mathbf{x}, \omega_i, \omega_o) L_i(\mathbf{x}, \omega_i) \cos \theta_i d\omega_i, \quad (1)$$

where $L_o(\mathbf{x}, \omega_o)$ is the radiance leaving point \mathbf{x} in direction ω_o , $L_e(\mathbf{x}, \omega_o)$ is the emitted radiance at \mathbf{x} in direction ω_o , $f_r(\mathbf{x}, \omega_i, \omega_o)$ is the BRDF term, $L_i(\mathbf{x}, \omega_i)$ is the incoming

radiance at point \mathbf{x} from direction ω_i , and θ_i is the angle between the normal at point \mathbf{x} and direction ω_i .

3. Methodology

3.1. Overview

Our proposed method addresses the challenging problem of decomposing light into physically based rendering (PBR) materials such as albedo and roughness for a set of posed images with strong shadows and indirect illumination. As shown in Fig. 2, our framework utilizes a robust training scheme consisting of four sequential phases. First, we obtain an implicit representation of the scene and radiance fields $S(x, \omega)$ using NeuS [47]. Second, we optimize the noisy normal field obtained from the first stage (Sec. 3.2). Third, we employ a compact visibility representation, which we then utilize to learn a masked indirect radiance field to facilitate the convergence (Sec. 3.3). Finally, we decompose the light into albedo, roughness, and environment light with a non-linearly mapped indirect radiance field (Sec. 3.4). Additionally, we refine the previously learned visibility and normal through regularized estimation, which addresses geometric inaccuracies and improves convergence stability (Sec. 3.5).

3.2. Optimize Noisy Normal Field

During the factorization process, we observed that the presence of noise in the normal field, which was introduced by the reconstruction step using NeuS, had a significant impact on visibility prediction, indirect illumination representation, and subsequent decomposition results. To address this issue, we drew inspiration from Ref-NeRF [45] and Mip-NeRF [3], and used an MLP to obtain the normal field with reduced noises. We also refine the mesh extracted from NeuS using traditional mesh-processing algorithms, such as repairing (*merge close vertices and remove duplicated faces*) and simplification in MeshLab to reduce geometry noise and accelerate computation. In addition to employing the \mathcal{L}_2 loss, we also incorporated a smooth loss to further reduce noise and enhance the quality of the normal:

$$\mathcal{L}_{norm} = \frac{1}{N} (\|n - \hat{n}\|_2^2 + \|n - n'\|_2^2), \quad (2)$$

where n denotes the normal learned by MLP, \hat{n} denotes the supervision value introduced by the mesh extracted from NeuS, and n' is a smooth term by adding $0.02 \times$ gaussian noises to n .

3.3. Masked Indirect Light With Visibility

InvRender [57] models indirect radiance field $L_I(x, \omega_i)$ at the intersection x of the camera ray and surface along direction ω_i by first performing ray tracing, then assigned

by the out-going radiance $S_o(\hat{x}, -\omega_i)$ at the second intersection point \hat{x} toward direction $-\omega_i$, and finally transfer it into SG parameters. However, this approach often results in an indirect illumination representation that is too smooth to accurately capture the nuances of the actual lighting field. A visualization and detailed analysis of our method can be found in Fig. 11. We observed a notable "learning trap", along with a darkened indirect illumination at the boundaries, leading to residual indirect illumination in the albedo. This issue stems from the inherent conflict between the smoothness of the SG basis functions and the discontinuous nature of indirect illumination.

To address the aforementioned issue, we propose a masked method that separates the over-smooth indirect radiance field into occlusion and non-occlusion parts using a learnable visibility network. Non-occlusion parts refer to the rays that pass through an object with only one bounce. By only optimizing the occlusion part of the indirect radiance field, we can model indirect illumination more accurately.

The calculation of visibility is a critical step in indirect illumination training. However, performing sphere tracing at surface points requires a significant amount of time and memory. To overcome this limitation, we use an octree tracer extracted from SDF to accelerate the tracing and obtain more precise intersection results. In addition, we followed [57] to improve efficiency by compressing the visibility field into an MLP that maps the surface point location \mathbf{x} and direction ω to visibility $V(\mathbf{x}, \omega)$, providing a compact and continuous representation. Then, the indirect light L_I with a mixture of $M = 24$ SGs can be divided by visibility:

$$L_I(\mathbf{x}, \omega; \Gamma) = (1 - V(\mathbf{x}, \omega)) \sum_{j=1}^M G(\omega; \Gamma_j(\mathbf{x}, \gamma)), \quad (3)$$

$$G(\omega; \xi, \lambda, \mu) = \mu e^{\lambda(\omega \cdot \xi - 1)},$$

where we use MLP Γ to output the j th SG parameters ($\xi \in R^3$ is the lobe axis, $\lambda \in R^1$ is the lobe sharpness, and $\mu \in R^3$ is the lobe amplitude), G denotes function of spherical Gaussians, and γ denotes the scale factor, which will be illustrated in Sec. 3.4.

The indirect radiance field is supervised by the color of the second intersection sample \hat{x} from the implicit radiance fields $S(\hat{x}, \omega)$ learned by NeuS. To enhance the convergence stability, we use *softplus* as the activation function. \mathcal{L}_{indir} and \mathcal{L}_{vis} are optimized by \mathcal{L}_1 and binary cross entropy loss as follows:

$$\mathcal{L}_{indir} = \frac{1}{N} \|\hat{L}_I - L_I\|_1, \quad (4)$$

$$\mathcal{L}_{vis} = \frac{1}{N} \sum_{i=1}^N BCE(V(\mathbf{x}, \omega) \parallel \hat{V}(\mathbf{x}, \omega)),$$

where $BCE(p_i \| y_i) = y_i \cdot \log(p_i) + (1 - y_i) \log(1 - p_i)$, \hat{L}_I is obtained by querying NeuS, and $\hat{V}(\mathbf{x}, \boldsymbol{\omega})$ is obtained by the octree tracer from point \mathbf{x} along direction $\boldsymbol{\omega}$.

3.4. Decomposition with Non-linearly Mapped Indirect Radiance Field

During the scene decomposition stage, we use differentiable rendering to factorize the scene’s materials and adopt $M = 128$ learnable SGs to model direct environment light. However, previous approaches tend to leave shadow and indirect illumination in albedo under scenes with high light intensity, which necessitate decreasing and increasing illumination in the corresponding regions to eliminate. Therefore, we need to apply a non-linear mapping to the light, making the light intensity weaker in shadowed areas and stronger in reflection areas. Inspired by [30], we apply HDR tone mapping to the masked indirect radiance field mentioned in Sec. 3.3 and the direct light learned at this stage will be transformed into the same value domain as the non-linear mapping of the indirect radiance field.

HDR Tone Mapping Several recent works [16, 30] have incorporated HDR into NeRF for specific applications. We adopt the widely used Academy Color Encoding System (ACES) [1] tone mapping. Specifically, we apply the ACES tone mapping function \mathcal{F} to the input HDR color e , which is formulated as:

$$\mathcal{F}(e) = \frac{(2.51e + 0.03)e}{(2.43e + 0.59)e + 0.14}, \quad (5)$$

whereas for the input LDR color c , we use the ACES inverse tone mapping function \mathcal{F}_I , which is given by:

$$\mathcal{F}_I(c) = \frac{0.59c - 0.03 + \sqrt{-1.0127c^2 + 1.3702c + 0.0009}}{2(2.51 - 2.43c)}. \quad (6)$$

Automatic ACES tone mapping search Since the lighting intensity of different scenes varies, ACES tone mapping cannot be applied to all scenes. To address this, we introduce an additional learnable parameter $\gamma \in (0, 1]$, which deforms the ACES tone mapping curve to automatically adapt to each scene. The deformed tone mapping function is defined as follows:

$$\begin{aligned} \mathcal{F}^\gamma(e) &= \text{clip}(\gamma^{-0.2} \mathcal{F}(e); 0, 1), \\ \mathcal{F}_I^\gamma(c) &= \text{clip}(\mathcal{F}_I(c \cdot \gamma^{0.2}); 0, 1). \end{aligned} \quad (7)$$

However, simultaneous training of the indirect radiance field with varying γ and the material decomposition model is challenging. To overcome this issue, we separate the scene-specific gamma learning into two stages. In the first

stage, as shown in Equ. 3, we train the indirect radiance field by treating γ as an explicit input, randomly sampling all possible values of γ . Consequently, the loss function \mathcal{L}_{indir} in Equ. 4 is then revised to include γ as follows:

$$\mathcal{L}_{indir} = \frac{1}{N} \|\mathcal{F}_I^\gamma(\hat{L}_I) - L_I\|_1. \quad (8)$$

Up to this point, we obtain the non-linearly mapped indirect radiance field with coefficient γ . We then stop training the indirect radiance field and treat γ as a learnable parameter. The optimal γ for the current scene will be determined as the decomposition model converges.

Material Decomposition In order to generate physically correct materials, it is necessary to introduce rendering equation priors to constrain the output of the network. Following the work by [57], we represent PBR materials as an encoder-decoder network and employ the simplified Disney BRDF [8]. The network initially encodes the input surface point \mathbf{x} into its corresponding latent code \mathbf{z} and subsequently decodes it into albedo and roughness. These values are then input into the BRDF $f_r(a, r)$ to generate the final rendered image, with the network’s output supervised through the BRDF prior.

To simplify the computation, we assume dielectric materials with a fixed value of $F_0 = 0.02$ for the Fresnel term. To further reduce the occurrence of noise and cracks, we also add a smooth loss to the albedo and roughness, as specified in Equ. 2.

3.5. Regularized Visibility Estimation

One of our primary goals is to achieve clean albedo with no residual shadows, which are typically caused by direct lighting and inaccurate visibility. Despite all efforts of the previous stages, a small amount of stubborn visibility errors caused by reflectance still exist, affecting the actual contribution of direct light.

To this end, we introduce a prior assumption stating that “the visibility ratio of a specific point \mathbf{x} from a given direct SG is smooth” to further optimize visibility, and present regularized visibility estimation (RVE) that utilizes an intermediate layer $\tilde{Q}(\mathbf{x}, \boldsymbol{\tau})$ to jointly optimize against the previously learned visibility network $V(\mathbf{x}, \boldsymbol{\omega})$. Specifically, $\tilde{Q}(\mathbf{x}, \boldsymbol{\tau})$ is a visibility prediction network learned from scratch, indicating the visibility ratio of point \mathbf{x} to the direct SG, while $\boldsymbol{\tau}$ represents the one-hot embedding of each direct SG. Since visibility errors primarily occur at the edges and boundaries, which are also sparse in the scene, we leverage the following sparse loss to make the residual sparse:

$$\begin{aligned} \mathcal{L}_{sparse} &= \text{KL}(\tilde{Q}(\mathbf{x}, \boldsymbol{\tau}) - \eta(\mathbf{x}) \| \epsilon), \\ \eta &= \frac{\sum_{i=0}^S G(\boldsymbol{\omega}_i) V(\mathbf{x}, \boldsymbol{\omega}_i)}{\sum_{i=0}^S G(\boldsymbol{\omega}_i)}, \end{aligned} \quad (9)$$

where $\text{KL}(P \parallel \hat{P}) = P \log \frac{P}{\hat{P}} + (1-P) \log \frac{1-P}{1-\hat{P}}$ represents Kullback-Leibler divergence loss that measures the relative entropy of two probability distributions, ϵ represents a constant distribution function returning 0.01, and η signifies the same concept as in InvRender, with the visibility ratio for direct SGs obtained by randomly sampling $S = 8$ directions.



Figure 3. Visualization of masked direct light SGs. We run experiments to visualize masked direct light SG before and after regularized visibility estimation. Persistent visibility errors result in incorrect masks at shadow boundaries, which are critical for removing shadows in albedo. We optimize visibility errors by using regularized visibility estimation to provide direct light SGs with more accurate masks for decomposition.

The regularized visibility estimation creates a gradient between $Q(\mathbf{x}, \tau)$ and the octree-based visibility caching network $V(\mathbf{x}, \omega)$. Furthermore, it makes training more flexible and less sensitive to regularization weights with two different optimizing directions. As the two components gradually converge through regularized visibility estimation, a more accurate visibility $V(\mathbf{x}, \omega)$ can be obtained for decomposition (See in Fig. 3). We also apply the same regularized estimation strategy to the normal field learned in the normal optimizing stage to obtain a more accurate normal.

After incorporating regularized visibility estimation into inverse rendering, our final loss function in the decomposition stage is:

$$\mathcal{L} = \lambda_{rgb} \mathcal{L}_{rgb} + \lambda_{sm} \mathcal{L}_{sm} + \lambda_{KL} \mathcal{L}_{KL}, \quad (10)$$

where \mathcal{L}_{rgb} is the \mathcal{L}_2 loss for reconstruction, \mathcal{L}_{sm} is the same smooth \mathcal{L}_1 loss as Equ. 2 for albedo and roughness, and \mathcal{L}_{KL} is the KL divergence between the latent code of BRDF and zero.

4. Experiments

In this section, we present the experimental evaluation of our methods. To assess the effectiveness of our approach, we collect synthetic and real datasets from NeRF and NeuS without any post-processing. In addition, we use Blender to render our own datasets to further demonstrate the superiority of our methods. The collected datasets are used to evaluate the performance of our methods in terms of reconstruction accuracy and decomposition quality.

Our model hyperparameters consisted of a batch size of 1024, with each stage trained for 100 epochs and 200k iterations for the NeuS training. For regularized visibility estimation, we initialized \tilde{Q} for the first 5 epochs. The model was implemented in PyTorch and optimized with the Adam optimizer at a learning rate of $5e^{-4}$. All tests were conducted on a single Tesla V100 GPU with 32GB of global memory. The training time without NeuS is around 5 hours.

4.1. Decomposition Results and Comparisons

We evaluate the performance of our proposed methods by comparing them to three closely related inverse rendering methods that all decompose scenes under unknown illumination conditions: InvRender [57], TensoIR [17], NeRO [26], NeRFactor [56], and NVDiffrec [33].

As shown in Fig. 4, our method removes shadows more effectively and produces cleaner albedo and roughness. In comparison with other methods, our method produces smoother results without losing details. Additional results can be found in Fig. 9 and 10. Quantitative evaluations provided in Tab. 1 show the precision of the albedo. The term "Log" refers to the sigmoid tone mapping used during these evaluations. Our approach ensures satisfactory performance in both reconstruction and decomposition quality. It should be noted that NVDiffrec tends to overly sacrifice albedo quality for ultimate reconstruction accuracy.

The reconstructed environment light maps are shown in Fig. 5, where the lighting is shifted by a constant on exposure to visualize the HDR values. Our method can more accurately estimate the position of the light source and generate higher and more precise light intensity in HDR environment.

We also perform experiments on real-world captured scenes. As illustrated in Fig. 9, our method is capable of decomposing real-world objects into plausible geometry, albedo, and roughness. Decomposed components can be used to aid in downstream tasks such as realistically relighting real-world scenes under arbitrary lighting conditions for free-viewpoint navigation.

4.2. Ablation Studies

We perform an ablation study to analyze the importance of the key components in our proposed *SIRe-IR* methods. As illustrated in Fig. 6, we observe that InvRender produces poor decomposition results under intense lighting conditions. This is due to the lack of non-linear mapping for the radiance fields in InvRender, which inhibits it from effectively balancing the light intensity, thereby leaving residual shadows and indirect illumination. In the absence of ACES tone mapping, our method is unable to eliminate both shadows and indirect illumination. Without regularized visibility estimation, the training process is frequently unstable

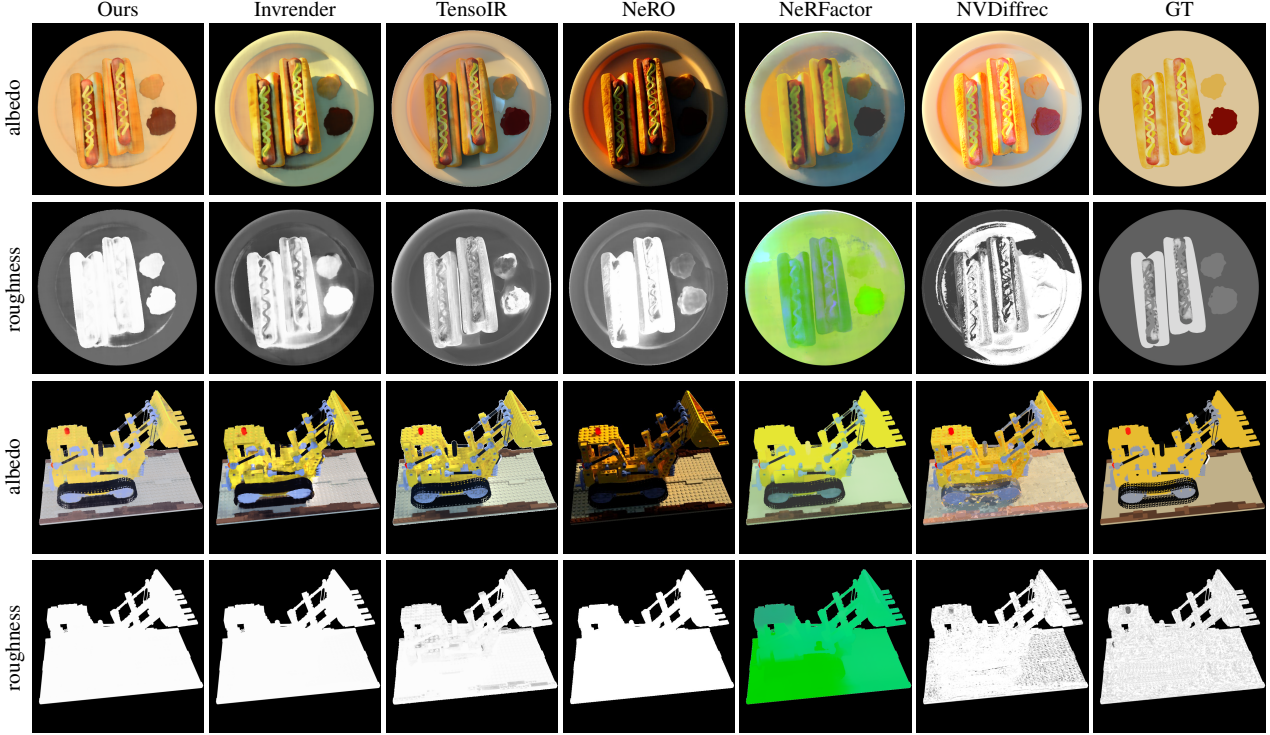


Figure 4. **Comparisons to state-of-the-art methods.** We compare our method to several previous approaches, including InvRender [57], TensoIR [17], NeRO [26], NeRFactor [56], and NVDiffrec [14]. The results show that our method outperforms previous approaches in the accuracy of albedo and roughness generation. We should note that NeRFactor does not explicitly model roughness, so we represent it with the corresponding BRDF latent code. Furthermore, we train NVDiffrec from scratch rather than using a pre-trained mesh for initialization.

Scene	Albedo (SSIM) \uparrow				Albedo (LPIPS) \downarrow				Roughness (SSIM) \uparrow			
	Hotdog	Lego	Helmet	Chess	Hotdog	Lego	Helmet	Chess	Hotdog	Lego	Helmet	Chess
ours-ACES	0.9283	0.8941	0.9461	0.8535	0.1636	0.1367	0.1152	0.1884	0.9190	0.8823	0.8583	0.8101
ours-Log	0.9046	0.8863	0.9276	0.8354	0.1941	0.1389	0.1071	0.2013	0.8248	0.8805	0.8356	0.6837
no hdr	0.9041	0.8933	0.9056	0.8524	0.1972	0.1382	0.1457	0.2029	0.8870	0.8803	0.8819	0.6374
no reg-estim	0.9157	0.8871	0.9383	0.8198	0.1992	0.1368	0.1224	0.2387	0.8985	0.8804	0.8441	0.8779
InvRender	0.8762	0.8833	0.9115	0.8126	0.2275	0.1551	0.1509	0.2259	0.8842	0.8807	0.8900	0.7083
TensoIR	0.8115	0.8154	0.7874	0.7504	0.2047	0.1896	0.1827	0.1805	0.7931	0.7349	0.7613	0.6871
nvdiffrc	0.8377	0.7872	0.7859	0.7363	0.3649	0.2785	0.3454	0.4060	0.7351	0.8148	0.7796	0.8194
nerfactor	0.8238	0.8386	-	-	0.3318	0.2208	-	-	-	-	-	-

Table 1. **Quantitative evaluations.** We present the results of four synthetic scenes. We color each cell as **best** and **second best**. Due to specific component naming rules in the Blender scene, we only compared datasets that NeRFactor supports. In summary, our method can produce high-quality albedo and roughness while maintaining the reconstruction fidelity.

and the resulting albedo may contain shadows in the corners and boundaries. The "Log Tone" result indicates that ACES offers a more effective non-linear mapping than the sigmoid function within our framework. Finally, our full method, which integrates all key components, can correctly decompose light into albedo and roughness, resulting in the best performance.

4.3. Application

De-shadowing De-shadowing is a challenging task in the field of inverse rendering, often requiring strong priors and large data-driven models. Our proposed method correctly understands various lighting effects and is capable of effectively eliminating strong and irregular shadows, particularly in scenes with intense lighting. As shown in Fig. 7, by setting the visibility ratio η to 1, we remove the shadowed portions caused by direct light occlusion. It should be noted that our method cannot remove the areas with re-

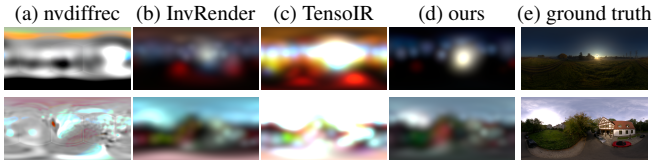


Figure 5. **Reconstructed environment light map.** We present the reconstructed environment maps of two synthetic scenes, the hotdog (upper) and the helmet (bottom). Compared to existing approaches, our method produces superior environment light perception, indicating its effectiveness in modeling non-linearly mapped radiance fields.

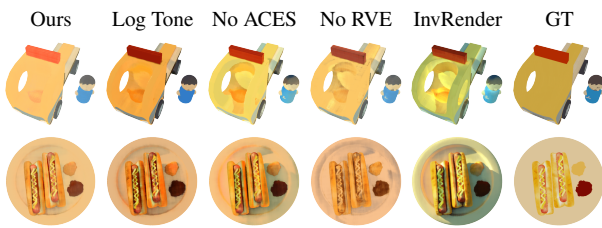


Figure 6. **Ablation Study.** We conduct ablation experiments on the key components in the Scene Decomposition Stage, with "Log Tone" referring to the use of sigmoid tone mapping as opposed to ACES tone mapping. The ablation results not only validate the effectiveness of ACES non-linear tone mapping but also emphasize the critical importance of each component in our proposed framework for attaining high-quality albedo.

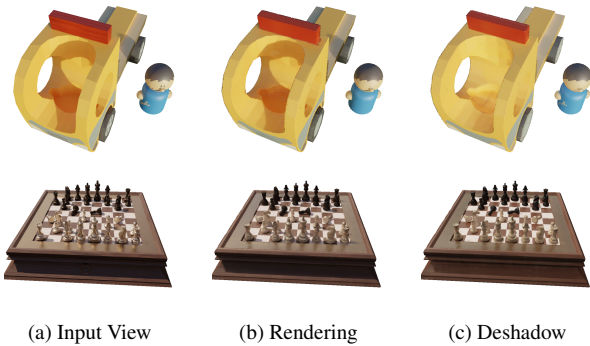


Figure 7. **De-shadowing.** We showcase the effectiveness of our method in de-shadowing applications. Given an input image captured from a specific viewpoint (a), our proposed approach can accurately remove shadows caused by direct light occlusion (c) even in challenging scenes with intense illumination, while preserving high-fidelity in the re-rendered results (b).

lections and the dark regions caused by the backlighting phenomenon. But this also to some extent demonstrates the accuracy of our method's visibility. These results also demonstrate the ability of our model to accurately identify and remove unwanted shadows.

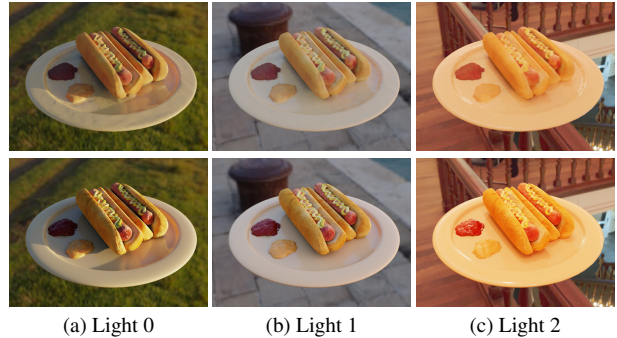


Figure 8. **Relighting.** We employ Blender to relight the extracted mesh, where the first row denotes our predictions, and the second row represents GT. Our approach allows for relighting the scene with decomposed components, providing flexibility to modify the lighting conditions as desired.

Relighting To demonstrate the practical utility of the materials derived from our method, we performed relighting experiments. We can directly use the meshes and textures obtained from our workflow for relighting. The relighting results, shown in Fig. 8, illustrate the ability of our decomposition results to accurately render in different lighting environments.

5. Conclusions and Discussions

We presented a novel inverse rendering framework for extracting high-quality albedo and roughness by removing shadows and indirect illumination. The key innovation lies in the use of non-linear mapping (ACES tone mapping) for illumination, which eliminates shadows and indirect illumination at the same time. In addition, masked indirect illumination and regularized visibility estimation are employed to ensure the high quality of decomposition. Experiment results on both synthetic and real data show that our full framework outperforms previous work in eliminating shadows and indirect illumination in PBR materials. Furthermore, scene components such as albedo, roughness, normal, and environment light produced in our method can be directly used in the traditional render pipeline.

Currently, the proposed method has some limitations. First, areas with strong reflections pose a significant challenge for accurate processing, which leads to artifacts in the corresponding regions in albedo and normal. Second, objects with non-solid surfaces, translucent objects, and thin objects cannot be correctly handled due to the limitations of NeuS. Third, the employment of SGs to model both direct and indirect lighting presents challenges in dealing with anisotropic objects, consequently leading to our method's deficiency in incorporating the metallic learnable parameters present in the Disney BRDF model [8]. Finally, we have not considered scenes with dynamic lighting. We can

draw inspiration from [28, 44] to adapt to such scenarios in future work.

References

[1] Walter Arrighetti. The academy color encoding system (aces): A professional color-management framework for production, post-production and archival of still and motion pictures. *Journal of Imaging*, 3(4):40, 2017. 5

[2] Jonathan T Barron and Jitendra Malik. Shape, illumination, and reflectance from shading. *IEEE Transactions on Pattern Analysis and Machine Intelligence*, 37(8):1670–1687, 2014. 3

[3] Jonathan T Barron, Ben Mildenhall, Matthew Tancik, Peter Hedman, Ricardo Martin-Brualla, and Pratul P Srinivasan. Mip-nerf: A multiscale representation for anti-aliasing neural radiance fields. In *Proceedings of the IEEE/CVF International Conference on Computer Vision*, pages 5855–5864, 2021. 4

[4] Mark Boss, Raphael Braun, Varun Jampani, Jonathan T Barron, Ce Liu, and Hendrik Lensch. Nerd: Neural reflectance decomposition from image collections. In *Proceedings of the IEEE/CVF International Conference on Computer Vision*, pages 12684–12694, 2021. 2, 3

[5] Mark Boss, Andreas Engelhardt, Abhishek Kar, Yuanzhen Li, Deqing Sun, Jonathan Barron, Hendrik Lensch, and Varun Jampani. Samurai: Shape and material from unconstrained real-world arbitrary image collections. *Advances in Neural Information Processing Systems*, 35:26389–26403, 2022. 3

[6] Mark Boss, Varun Jampani, Raphael Braun, Ce Liu, Jonathan Barron, and Hendrik Lensch. Neural-pil: Neural pre-integrated lighting for reflectance decomposition. *Advances in Neural Information Processing Systems*, 34:10691–10704, 2021. 3

[7] Mark Boss, Varun Jampani, Kihwan Kim, Hendrik Lensch, and Jan Kautz. Two-shot spatially-varying brdf and shape estimation. In *Proceedings of the IEEE/CVF Conference on Computer Vision and Pattern Recognition*, pages 3982–3991, 2020. 3

[8] Brent Burley and Walt Disney Animation Studios. Physically-based shading at disney. In *Acm Siggraph*, volume 2012, pages 1–7. vol. 2012, 2012. 5, 8

[9] Anpei Chen, Zexiang Xu, Andreas Geiger, Jingyi Yu, and Hao Su. Tensorf: Tensorial radiance fields. In *European Conference on Computer Vision (ECCV)*, 2022. 3

[10] Ziyu Chen, Chenjing Ding, Jianfei Guo, Dongliang Wang, Yikang Li, Xuan Xiao, Wei Wu, and Li Song. L-tracing: Fast light visibility estimation on neural surfaces by sphere tracing. In *European Conference on Computer Vision*, pages 217–233. Springer, 2022. 2, 3

[11] Zhiqin Chen, Thomas Funkhouser, Peter Hedman, and Andrea Tagliasacchi. Mobilenerf: Exploiting the polygon rasterization pipeline for efficient neural field rendering on mobile architectures. *arXiv preprint arXiv:2208.00277*, 2022. 3

[12] Ziang Cheng, Hongdong Li, Yuta Asano, Yinqiang Zheng, and Imari Sato. Multi-view 3d reconstruction of a texture-less smooth surface of unknown generic reflectance. In *Proceedings of the IEEE/CVF Conference on Computer Vision and Pattern Recognition*, pages 16226–16235, 2021. 1, 3

[13] Stephan J Garbin, Marek Kowalski, Matthew Johnson, Jamie Shotton, and Julien Valentin. Fastnerf: High-fidelity neural rendering at 200fps. In *Proceedings of the IEEE/CVF International Conference on Computer Vision*, pages 14346–14355, 2021. 3

[14] Jon Hasselgren, Nikolai Hofmann, and Jacob Munkberg. Shape, Light, and Material Decomposition from Images using Monte Carlo Rendering and Denoising. *arXiv:2206.03380*, 2022. 1, 7

[15] Peter Hedman, Pratul P Srinivasan, Ben Mildenhall, Jonathan T Barron, and Paul Debevec. Baking neural radiance fields for real-time view synthesis. In *Proceedings of the IEEE/CVF International Conference on Computer Vision*, pages 5875–5884, 2021. 3

[16] Xin Huang, Qi Zhang, Ying Feng, Hongdong Li, Xuan Wang, and Qing Wang. Hdr-nerf: High dynamic range neural radiance fields. In *Proceedings of the IEEE/CVF Conference on Computer Vision and Pattern Recognition*, pages 18398–18408, 2022. 5

[17] Haian Jin, Isabella Liu, Peijia Xu, Xiaoshuai Zhang, Songfang Han, Sai Bi, Xiaowei Zhou, Zexiang Xu, and Hao Su. Tensoir: Tensorial inverse rendering. In *Proceedings of the IEEE/CVF Conference on Computer Vision and Pattern Recognition (CVPR)*, 2023. 1, 3, 6, 7

[18] James T Kajiya. The rendering equation. In *Proceedings of the 13th annual conference on Computer graphics and interactive techniques*, pages 143–150, 1986. 3

[19] Julian Knott, Joe Bartusek, Seung-Hwan Baek, and Felix Heide. Neural ray-tracing: Learning surfaces and reflectance for relighting and view synthesis. *arXiv preprint arXiv:2104.13562*, 2021. 2, 3

[20] Zhengfei Kuang, Kyle Olszewski, Menglei Chai, Zeng Huang, Panos Achlioptas, and Sergey Tulyakov. Neroic: Neural rendering of objects from online image collections. *ACM Trans. Graph.*, 41(4), jul 2022. 3

[21] Hendrik PA Lensch, Jan Kautz, Michael Goesele, Wolfgang Heidrich, and Hans-Peter Seidel. Image-based reconstruction of spatial appearance and geometric detail. *ACM Transactions on Graphics (TOG)*, 22(2):234–257, 2003. 3

[22] Tzu-Mao Li, Miika Aittala, Frédo Durand, and Jaakko Lehtinen. Differentiable monte carlo ray tracing through edge sampling. *ACM Transactions on Graphics (TOG)*, 37(6):1–11, 2018. 1

[23] Zhengqin Li, Mohammad Shafiei, Ravi Ramamoorthi, Kalyan Sunkavalli, and Manmohan Chandraker. Inverse rendering for complex indoor scenes: Shape, spatially-varying lighting and svbrdf from a single image. In *Proceedings of the IEEE/CVF Conference on Computer Vision and Pattern Recognition*, pages 2475–2484, 2020. 1

[24] Zhengqin Li, Zexiang Xu, Ravi Ramamoorthi, Kalyan Sunkavalli, and Manmohan Chandraker. Learning to reconstruct shape and spatially-varying reflectance from a single image. *ACM Transactions on Graphics (TOG)*, 37(6):1–11, 2018. 3

[25] Lingjie Liu, Jiatao Gu, Kyaw Zaw Lin, Tat-Seng Chua, and Christian Theobalt. Neural sparse voxel fields. *Advances in Neural Information Processing Systems*, 33:15651–15663, 2020. 3

[26] Yuan Liu, Peng Wang, Cheng Lin, Xiaoxiao Long, Jiepeng Wang, Lingjie Liu, Taku Komura, and Wenping Wang. Nero: Neural geometry and brdf reconstruction of reflective objects from multiview images. In *SIGGRAPH*, 2023. 3, 6, 7

[27] Julien N. P. Martel, David B. Lindell, Connor Z. Lin, Eric R. Chan, Marco Monteiro, and Gordon Wetzstein. Acorn: Adaptive coordinate networks for neural scene representation. *ACM Trans. Graph. (SIGGRAPH)*, 40(4), 2021. 3

[28] Ricardo Martin-Brualla, Noha Radwan, Mehdi SM Sajjadi, Jonathan T Barron, Alexey Dosovitskiy, and Daniel Duckworth. Nerf in the wild: Neural radiance fields for unconstrained photo collections. In *Proceedings of the IEEE/CVF Conference on Computer Vision and Pattern Recognition*, pages 7210–7219, 2021. 9

[29] Abhimitra Meka, Mohammad Shafiei, Michael Zollhöfer, Christian Richardt, and Christian Theobalt. Real-time global illumination decomposition of videos. *ACM Transactions on Graphics*, 40(3), aug 2021. 3

[30] Ben Mildenhall, Peter Hedman, Ricardo Martin-Brualla, Pratul P Srinivasan, and Jonathan T Barron. Nerf in the dark: High dynamic range view synthesis from noisy raw images. In *Proceedings of the IEEE/CVF Conference on Computer Vision and Pattern Recognition*, pages 16190–16199, 2022. 5

[31] Ben Mildenhall, Pratul P. Srinivasan, Matthew Tancik, Jonathan T. Barron, Ravi Ramamoorthi, and Ren Ng. Nerf: Representing scenes as neural radiance fields for view synthesis. In *ECCV*, 2020. 1, 3

[32] Thomas Müller, Alex Evans, Christoph Schied, and Alexander Keller. Instant neural graphics primitives with a multiresolution hash encoding. *ACM Trans. Graph.*, 41(4):102:1–102:15, July 2022. 3

[33] Jacob Munkberg, Jon Hasselgren, Tianchang Shen, Jun Gao, Wenzheng Chen, Alex Evans, Thomas Müller, and Sanja Fidler. Extracting triangular 3d models, materials, and lighting from images. In *Proceedings of the IEEE/CVF Conference on Computer Vision and Pattern Recognition*, pages 8280–8290, 2022. 1, 6

[34] Merlin Nimier-David, Zhao Dong, Wenzel Jakob, and Anton Kaplanyan. Material and lighting reconstruction for complex indoor scenes with texture-space differentiable rendering. 2021. 1, 3

[35] Michael Oechsle, Songyou Peng, and Andreas Geiger. Unisurf: Unifying neural implicit surfaces and radiance fields for multi-view reconstruction. In *Proceedings of the IEEE/CVF International Conference on Computer Vision*, pages 5589–5599, 2021. 3

[36] Christian Reiser, Songyou Peng, Yiyi Liao, and Andreas Geiger. Kilonerf: Speeding up neural radiance fields with thousands of tiny mlps. In *Proceedings of the IEEE/CVF International Conference on Computer Vision*, pages 14335–14345, 2021. 3

[37] Shen Sang and Manmohan Chandraker. Single-shot neural relighting and svbrdf estimation. In *European Conference on Computer Vision*, pages 85–101. Springer, 2020. 3

[38] Carolin Schmitt, Simon Donne, Gernot Riegler, Vladlen Koltun, and Andreas Geiger. On joint estimation of pose, geometry and svbrdf from a handheld scanner. In *Proceedings of the IEEE/CVF Conference on Computer Vision and Pattern Recognition*, pages 3493–3503, 2020. 3

[39] Soumyadip Sengupta, Jinwei Gu, Kihwan Kim, Guilin Liu, David W Jacobs, and Jan Kautz. Neural inverse rendering of an indoor scene from a single image. In *Proceedings of the IEEE/CVF International Conference on Computer Vision*, pages 8598–8607, 2019. 1, 3

[40] Shuang Song and Rongjun Qin. A novel intrinsic image decomposition method to recover albedo for aerial images in photogrammetry processing, 2022. 3

[41] Pratul P Srinivasan, Boyang Deng, Xiuming Zhang, Matthew Tancik, Ben Mildenhall, and Jonathan T Barron. Nerv: Neural reflectance and visibility fields for relighting and view synthesis. In *Proceedings of the IEEE/CVF Conference on Computer Vision and Pattern Recognition*, pages 7495–7504, 2021. 3

[42] Cheng Sun, Min Sun, and Hwann-Tzong Chen. Direct voxel grid optimization: Super-fast convergence for radiance fields reconstruction. In *Proceedings of the IEEE/CVF Conference on Computer Vision and Pattern Recognition*, pages 5459–5469, 2022. 3

[43] Cheng Sun, Min Sun, and Hwann-Tzong Chen. Improved direct voxel grid optimization for radiance fields reconstruction. *arXiv preprint arXiv:2206.05085*, 2022. 3

[44] Jiaming Sun, Xi Chen, Qianqian Wang, Zhengqi Li, Hadar Averbuch-Elor, Xiaowei Zhou, and Noah Snavely. Neural 3d reconstruction in the wild. In *ACM SIGGRAPH 2022 Conference Proceedings*, pages 1–9, 2022. 9

[45] Dor Verbin, Peter Hedman, Ben Mildenhall, Todd Zickler, Jonathan T Barron, and Pratul P Srinivasan. Ref-nerf: structured view-dependent appearance for neural radiance fields. In *2022 IEEE/CVF Conference on Computer Vision and Pattern Recognition (CVPR)*, pages 5481–5490. IEEE, 2022. 4

[46] Delio Vicini, Sébastien Speierer, and Wenzel Jakob. Differentiable signed distance function rendering. *ACM Transactions on Graphics (TOG)*, 41(4):1–18, 2022. 1

[47] Peng Wang, Lingjie Liu, Yuan Liu, Christian Theobalt, Taku Komura, and Wenping Wang. Neus: Learning neural implicit surfaces by volume rendering for multi-view reconstruction. *NeurIPS*, pages 27171–27183, 2021. 2, 3, 4

[48] Wenqi Yang, Guanying Chen, Chaofeng Chen, Zhenfang Chen, and Kwan-Yee K Wong. Ps-nerf: Neural inverse rendering for multi-view photometric stereo. In *Computer Vision–ECCV 2022: 17th European Conference, Tel Aviv, Israel, October 23–27, 2022, Proceedings, Part I*, pages 266–284. Springer, 2022. 3

[49] Yao Yao, Jingyang Zhang, Jingbo Liu, Yihang Qu, Tian Fang, David McKinnon, Yanghai Tsin, and Long Quan. Neifl: Neural incident light field for physically-based material estimation. In *Computer Vision–ECCV 2022: 17th European Conference, Tel Aviv, Israel, October 23–27, 2022, Proceedings, Part XXXI*, pages 700–716. Springer, 2022. 3

[50] Lior Yariv, Yoni Kasten, Dror Moran, Meirav Galun, Matan Atzmon, Basri Ronen, and Yaron Lipman. Multiview neural surface reconstruction by disentangling geometry and appearance. *Advances in Neural Information Processing Systems*, 33:2492–2502, 2020. 3

[51] Alex Yu, Ruilong Li, Matthew Tancik, Hao Li, Ren Ng, and Angjoo Kanazawa. Plenocubes for real-time rendering of neural radiance fields. In *Proceedings of the IEEE/CVF International Conference on Computer Vision*, pages 5752–5761, 2021. 3

[52] Ye Yu and William AP Smith. Inverserendernet: Learning single image inverse rendering. In *Proceedings of the IEEE/CVF Conference on Computer Vision and Pattern Recognition*, pages 3155–3164, 2019. 3

[53] Jason Zhang, Gengshan Yang, Shubham Tulsiani, and Deva Ramanan. Ners: neural reflectance surfaces for sparse-view 3d reconstruction in the wild. *Advances in Neural Information Processing Systems*, 34:29835–29847, 2021. 1

[54] Kai Zhang, Fujun Luan, Zhengqi Li, and Noah Snavely. Iron: Inverse rendering by optimizing neural sdfs and materials from photometric images. In *Proceedings of the IEEE/CVF Conference on Computer Vision and Pattern Recognition*, pages 5565–5574, 2022. 3

[55] Kai Zhang, Fujun Luan, Qianqian Wang, Kavita Bala, and Noah Snavely. Physg: Inverse rendering with spherical gaussians for physics-based material editing and relighting. In *Proceedings of the IEEE/CVF Conference on Computer Vision and Pattern Recognition*, pages 5453–5462, 2021. 2, 3

[56] Xiuming Zhang, Pratul P Srinivasan, Boyang Deng, Paul Debevec, William T Freeman, and Jonathan T Barron. Nerfactor: Neural factorization of shape and reflectance under an unknown illumination. *ACM Transactions on Graphics (TOG)*, 40(6):1–18, 2021. 2, 3, 6, 7

[57] Yuanqing Zhang, Jiaming Sun, Xingyi He, Huan Fu, Rongfei Jia, and Xiaowei Zhou. Modeling indirect illumination for inverse rendering. In *Proceedings of the IEEE/CVF Conference on Computer Vision and Pattern Recognition*, pages 18643–18652, 2022. 1, 2, 3, 4, 5, 6, 7

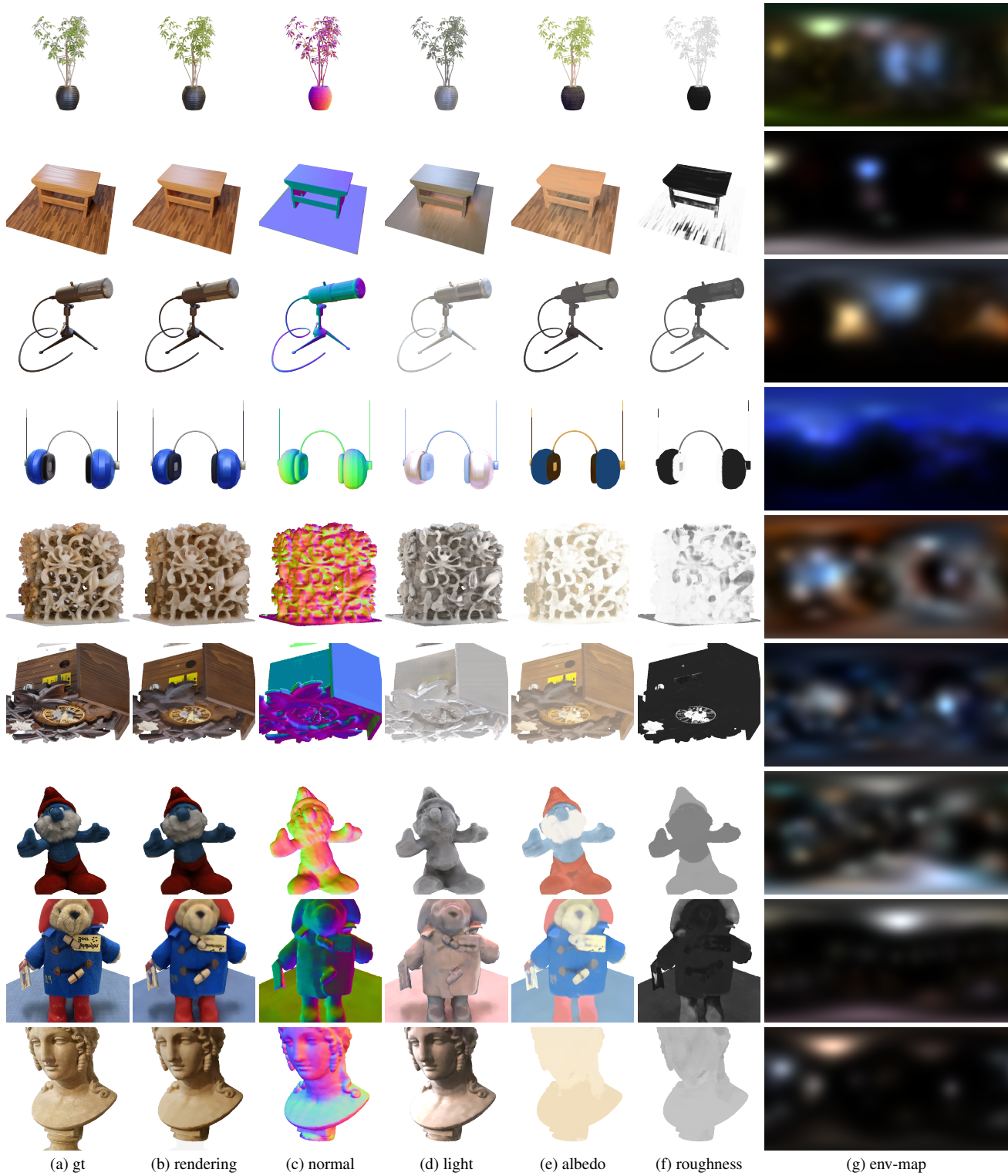


Figure 9. Other datasets' results. We present experimental results on various datasets, including four synthetic scenes and five real scenes. The first four rows in the results show the performance of our method in synthetic scenes, while the last five rows demonstrate its effectiveness on real scenes. In each dataset, we present the input ground-truth image (a), our rendering result (b), normal (c), light (d), albedo (e), and roughness (f) obtained through our method. These experiments illustrate the generalizability of our method across diverse datasets and demonstrate its ability to produce high-quality results.

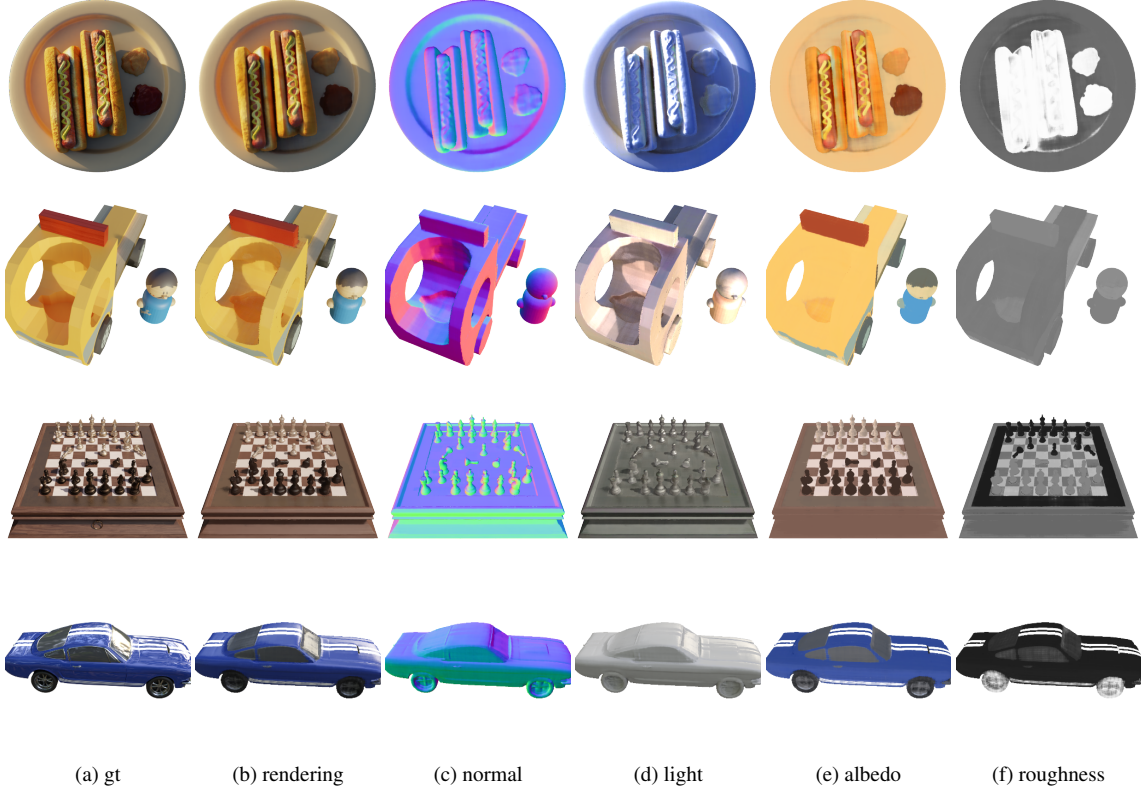


Figure 10. Results on synthetic datasets. We present additional results obtained from our method on several synthetic scenes, where we visualize the normal (c), light (d), albedo (e), and roughness (f) components, respectively. The fidelity of our method is further demonstrated by comparing the rendered results (b) with the ground truth images (a).

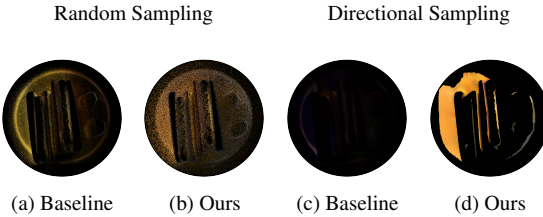


Figure 11. Visualization of masked indirect illumination. Our experimental results exhibit a notable enhancement in the representation of indirect light when comparing our masked indirect radiance field (L_I) to InvRender. While our approach predicts superior indirect light at boundaries by randomly sampling directions for indirect SGs, we noticed a significant difference under parallel direction sampling condition where we sample only a single specific direction for visualization. This discrepancy arises from the inherent contradiction between the smooth SG basis functions and the discontinuous indirect illumination. In the absence of masks, regions without indirect illumination will impact the learning and convergence of the SGs. As a result, there exists a "learning trap", where all SG coefficients diminish to zero. Our proposed approach adeptly addresses this issue, resulting in a more robust and accurate representation of the indirect radiance field.



Figure 12. Visualization of non-linearly mapped indirect radiance field. We conducted experiments to visualize the ACES-mapped indirect radiance field using different values of γ . Our results demonstrate that our method can accurately represent high-quality indirect illumination in scenes with natural light intensity, outperforming vanilla indirect radiance field. Furthermore, our deformable ACES tone mapping method can be applied to scenes under various lighting conditions, adapting to different γ . This showcases the versatility and robustness of our method in handling diverse scenarios, enhancing the overall quality for inverse rendering.